Prediction of monolayer FeP_4 with intrinsic half-metal ferrimagnetism above room temperature

Fanjunjie Han,[1] Xu Yan,[2] Fei Li,[2] Hong Yu,[1] Wenjing Li,[1] Xin Zhong,[3,*] Aitor Bergara,[4,5,6,†] and Guochun Yang[1,2,‡]

[1]*Centre for Advanced Optoelectronic Functional Materials Research and Key Laboratory for UV Light-Emitting Materials and Technology of Ministry of Education, Northeast Normal University, Changchun 130024, China*

[2]*State Key Laboratory of Metastable Materials Science & Technology and Key Laboratory for Microstructural Material Physics of Hebei Province, School of Science, Yanshan University, Qinhuangdao 066004, China*

[3]*Key Laboratory of Functional Materials Physics and Chemistry of the Ministry of Education, College of Physics, and National Demonstration Center for Experimental Physics Education, Jilin Normal University, Changchun 130103, People's Republic of China*

[4]*Physics Department and EHU-Quantum Center, University of the Basque Country, UPV/EHU, 48080 Bilbao, Spain*

[5]*Donostia International Physics Center (DIPC), 20018 Donostia, Spain*

[6]*Centro de Física de Materiales CFM, Centro Mixto CSIC-UPV/EHU, 20018 Donostia, Spain*

(Received 13 April 2022; revised 1 September 2022; accepted 20 December 2022; published 13 January 2023)

The design of high-temperature ferrimagnetic materials is highly demanded for next-generation functional spintronic devices. Here, we propose that the combination of nonmetallic structural units and magnetic atoms is an effective way to achieve high-temperature magnetism in two-dimensional (2D) materials. The predicted FeP_4 monolayer, consisting of quasisquare P_4 units, shows intrinsic half-metal ferrimagnetism above room temperature. Each Fe atom is coordinated with four P atoms associated with the surrounding four quasisquare P_4 units. First-principles calculations suggest that the FeP_4 monolayer presents a Curie temperature of 460 K. More interestingly, the itinerant electrons and the unique quasisquare P_4 units act as intermediaries and play an important role in promoting the Ruderman-Kittel-Kasuya-Yosida and superexchange interactions, respectively, which induces a robust ferrimagnetism. Our findings not only shed light on the promising future of 2D magnetic materials, but also are of interest for high-temperature spintronic applications.

DOI: 10.1103/PhysRevB.107.024414

I. INTRODUCTION

Spintronic devices, where spin of electrons is manipulated for faster information transmission and easier operation with a lower power consumption compared to traditional charge-based electronic ones, have become an exciting scientific research area [1–3]. Ferromagnets and antiferromagnets are the components that dominate spintronic devices, which take advantage of their interesting magnetic properties, such as macroscopic spontaneous magnetization in ferromagnets and robustness to magnetic-field disturbances in antiferromagnets [4–6]. However, there are still obvious shortcomings in their applications, i.e., ferromagnets usually trigger strong stray fields in devices and are very vulnerable to external magnetic fields, while the lack of macroscopic magnetization makes it difficult for antiferromagnets to work in integrated devices [7,8]. On the other hand, ferrimagnets combine the advantages of ferromagnets and antiferromagnets, i.e., easy operation in magnetic fields and ultrafast spin dynamics, benefiting from both net magnetic moments and antiferromagnetic coupling characteristics. Therefore, ferrimagnets are considered as another promising platform for spintronic materials and received great attention recently [9]. In fact, although experimental and theoretical works on ferrimagnets have developed rapidly in recent years [10–12], their low Curie temperature (T_C) imposes great limitations on their practical applications.

The confirmation of intrinsic magnetism of two-dimensional (2D) CrI_3 and $Cr_2Ge_2Te_6$ materials [13,14] injected again a new impetus in the exploration of 2D magnetic materials and the development of next-generation nanoscale spintronic devices with low power consumption, high integration, and better operability. Then, a large number of ferromagnetic and antiferromagnetic materials have been proposed, including ferromagnetic (FM) $CrBr_3$ [15], V_5Se_8 and Fe_3GeTe_2 [15,16], antiferromagnetic (AFM) MPS_3 (M = Fe, Mn, and Ni) [17], VI_3 and $MnBi_2Te_4$ [18,19]. Remarkably, recent reports of room-temperature ferromagnets, such as VSe_2 [20], $1T$-$CrTe_2$, and Cr_2Te_3 monolayers, provide a powerful support for the development of 2D spintronics [21,22]. In contrast, the experimental evidence and theoretical basis related to 2D ferrimagnetic (FIM) materials are scarce so far [23–27], and their low critical temperature greatly limits their applications. This motivates us to move forward in the design of the new 2D FIMs with desirable magnetic transition temperatures. A better understanding of their physical mechanism may provide a new strategy to find high-efficient spintronic nanodevices.

Iron (Fe), as the most representative ferromagnet, has attracted wide attention since its discovery, and the corresponding 2D counterpart, namely the Fe elemental monolayer,

*zhongxin@calypso.cn
†a.bergara@ehu.eus
‡yanggc468@nenu.edu.cn

has also been found to exhibit strong ferromagnetism [28,29]. Due to its unpaired electrons, Fe-based 2D compounds, made by combining Fe with different anionic ligands, also present excellent magnetic properties. For example, the Fe_3GeTe_2 monolayer is an itinerant ferromagnet with a large out-of-plane anisotropy [30]. The $FePS_3$ monolayer is an antiferromagnetic Mott insulator with a Néel temperature (T_N) of about 120 K [31]. Fe_2Si, FeB_3, and Fe_3P monolayers are ferromagnetic materials predicted to have a large perpendicular magnetic anisotropy and T_C as high as 780, 480, and 420 K, respectively [32–34]. Obviously, by selecting the appropriate nonmetal atoms, the formed 2D Fe-based system can still retain magnetism [35,36], which is of great importance for the study of 2D spintronics. In particular, in most studies there are isolated atoms [37–39], and not structural units, that act as mediators of magnetic exchange. However, the inclusion of structural units of main-group elements, with strong covalent bonds, cannot only improve the structural stability, but also induce an unexpected magnetism.

Phosphorus (P) has a modest electronegativity and the ability to form various structural units in their compounds [40]. Moreover, its three-coordination feature favors the stabilization of 2D materials, such as phosphorene, *b*-AsP, and SiP_2 [41–43]. Taking these factors into account, there is an expectation of forming stable P-rich magnetic 2D Fe-P compounds. In this paper, we systematically explore the 2D potential surface of P-rich Fe-P compositions through first-principles global structure search calculations. We have found a 2D half-metallic ferrimagnetic FeP_4 monolayer with unusual quasisquare P_4 units. Its high T_C and large magnetic anisotropic energy (MAE) indicate that the intrinsic long-range ferrimagnetic ordering can remain at high temperature, which is attributed to the quasisquare P_4 units promoting the magnetic exchange interaction. Our work could inspire the design of 2D magnetic materials with structural motifs.

II. COMPUTATIONAL DETAILS

Recently developed structural evolution algorithm can effectively find the ground state or metastable structures of a given chemical composition [44,45]. In this work, we apply the particle swarm optimization method, as implemented in the CALYPSO program, to explore the 2D potential surface of FeP_4 [46,47]. Its effectiveness has been verified in several systems [48–52]. The structural relaxation and electronic properties of FeP_4 were performed by using the density-functional theory within the Vienna *Ab initio* Simulation Package (VASP) [53]. Ion-electron interactions were described using the projector augmented-wave method, and the generalized gradient approximation (GGA) with the Perdew-Burke-Ernzerhof parametrization was adopted to approximate the exchange-correlation functional [54,55]. The cutoff energy of plane-wave expansions was chosen to be 500 eV, with an energy convergence precision of 10^{-6} eV. A vacuum region of >15 Å was considered to eliminate the interlayer interaction between supercells.

To reliably describe the strongly correlated *d* electrons of Fe atoms, we considered the GGA + *U* approximation in the magnetic and electronic calculations, where the effective on-site Coulomb interaction parameter (*U*) and exchange interaction parameter (*J*) were set to 2 and 0.95 eV, respectively, which is consistent with previously reported values [33,56]. For the magnetic energy difference and the MAE, the fully relativistic spin-orbit coupling was taken into account. Phonon dispersion curves were obtained from force constants calculated with the PHONOPY code using a 4 × 4 × 1 supercell [57]. *Ab initio* molecular-dynamics (AIMD) simulations were considered in a 5 × 5 × 1 supercell at 1000 K [58]. VASPKIT, the pre- and postprocessing tool for the VASP code, was used in our calculations [59]. The Curie temperature and specific-heat capacity were calculated with the MCSOLVER implementation [60]. The Supplemental Material includes information on the structure prediction and other computational details [61].

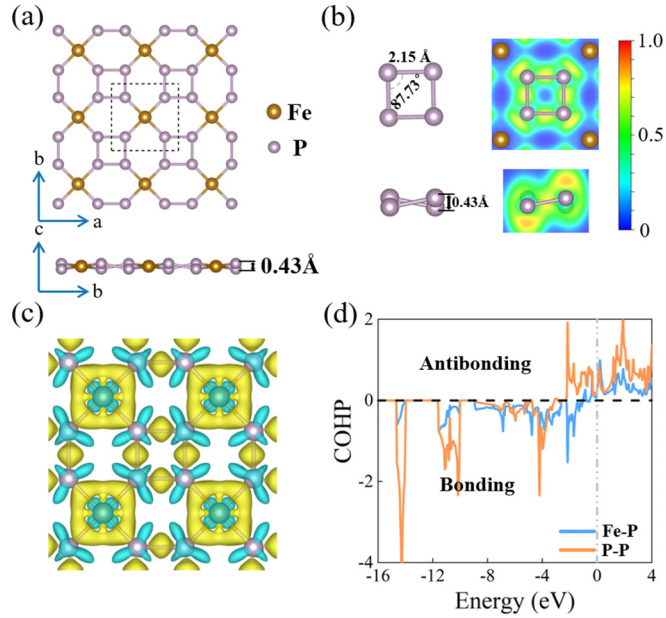

FIG. 1. (a) Top and side views of the FeP_4 monolayer with *P*-42*m* symmetry. The golden and pink balls represent Fe and P atoms, respectively. (b) Schematic diagram and the electron localization function map of the P_4 unit. (c) Charge-density difference for the FeP_4 monolayer. (d) Crystal orbital Hamilton population (COHP) curve of the adjacent Fe-P and P-P pairs in the FeP_4 monolayer.

III. RESULTS AND DISCUSSION

After a systemic structural search, the FeP_4 monolayer stabilizes into a tetragonal structure [space group $P-42m$ and one formula unit, Fig. 1(a)]. Its most striking feature is that the four equivalent P atoms form a unique quasisquare P_4 unit, and the Fe atom is coordinated with four P atoms contributed by the four identical P_4 units. Therefore, the basic building block of the FeP_4 monolayer is FeP_{16}. Three of the five valence electrons of a P atom in FeP_4, which has a three-coordinated configuration, are used to form the chemical bonds, and the remaining two act as lone pairs, repulsing each other and leading to the formation of a puckered structure. The four valence electrons of a Fe atom are used to form the chemical bonds with P atoms. The P–P and Fe–P bond lengths are slightly shorter than those in P allotropes and other Fe-P compounds (Table S1). On the other hand, the calculated electron localization function [Fig. 1(b)], charge-density

difference [Fig. 1(c)], and crystal orbital Hamilton population [Fig. 1(d), Table S2] clearly support the formation of strong P–P covalent and Fe–P ionic bonds.

Structural stability of compounds, including thermodynamic, dynamical, thermal, and mechanical stability, is closely related to their possible applications. The cohesive energy of the FeP_4 monolayer, an important magnitude for its thermodynamic stability and viability of experimental synthesis, was calculated as 3.73 eV per atom, which is slightly smaller but similar to FeP_3 (4.13 eV per atom) [72], Fe_2Si (4.10 eV per atom) [32], and Fe_3P (3.43 eV per atom) [33]. On the other hand, the FeP_4 monolayer sits on the convex hull of the Fe-P system (Fig. S1), indicating its thermodynamical stability with respect to Fe and P or other Fe-P monolayers. To explore the feasibility of its experimental synthesis, we have calculated the exfoliation energy (E_{ex}) of the FeP_4 monolayer deposition on the Au (111) surface (Fig. S2). The obtained E_{ex} is $1.03\,J/m^2$, which is comparable to the Ca_2N ($1.08\,J/m^2$) and GeP_3 ($1.14 J/m^2$) [73,74]. Thus, the FeP_4 monolayer could be prepared at proper conditions. The absence of imaginary phonon modes confirms its dynamic stability [Fig. S2(a)]. The highest frequency goes up to $566.73\,cm^{-1}$, contributed by P atoms, much higher than the highest frequencies of $470\,cm^{-1}$ in phosphorene [75], which confirms its strong P–P covalent bonds. The contribution of P atoms in phonons below 12.67 THz [Fig. S3(a)] shows a strong coupling between P and Fe atoms. Furthermore, its dynamical stability can be also preserved at 300 K (Fig. S4). Negligible structural fluctuations after AIMD simulations at 1000 K clearly demonstrate its high thermal stability [Fig. S3(b)].

To analyze the mechanical properties of the FeP_4 monolayer, we calculated its elastic constants: $C_{11} = C_{22} = 83.25\,N/m$, $C_{12} = 48.61\,N/m$, and $C_{66} = 55.71\,N/m$. Here, elastic constants are expressed in N/m, since there is no concept of volume for 2D materials and the stress of the material under strain is reflected on the line rather than on the plane; hence, the obtained elastic coefficients should be multiplied by the lattice constant in the direction of the vacuum layer. According to the Born criteria of 2D tetragonal materials [76,77], the standard mechanical stability is $C_{11}C_{22} - C_{12}^2 > 0$ and $C_{66} > 0$, indicating that the FeP_4 monolayer is mechanically stable. In addition, we also investigated the Young modulus $Y(\theta)$ and Poisson ratio $v(\theta)$ [Figs. S3(c) and S3(d)]. Both are anisotropic and $Y(\theta)$ varies from 55 to 121 N/m, which is comparable to that of phosphorene (24–102 N/m) and smaller than in MoS_2 (120–240 N/m) [78], indicating that FeP_4 presents a rigid bond network. Meanwhile, $v(\theta)$ varies from 0.08 to 0.58. In this sense, the FeP_4 monolayer has an interesting flexibility and excellent mechanical response.

Analysis of chemical bonds in the FeP_4 monolayer allows us to conclude that Fe atom keeps the remaining nonbonded electrons, which could induce interesting magnetic properties. Here, in order to determine the magnetic ground state of FeP_4 (see Fig. S5), four different magnetic configurations are considered in a $2 \times 2 \times 1$ supercell: a ferromagnetic (FM), two antiferromagnetic (AFM1 and AFM2), and another ferrimagnetic (FIM) state. Then, the structures of the FeP_4 monolayer are relaxed with the aforementioned four magnetic configurations and the relevant information is summarized in

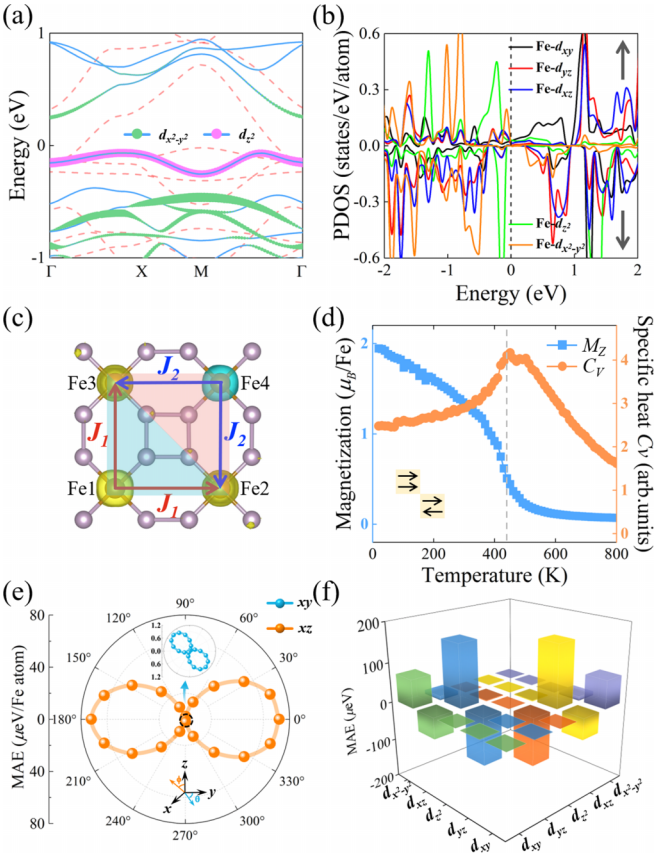

FIG. 2. (a) Spin-polarized band structure and (b) PDOS onto five partial d orbitals of Fe atoms for FeP_4. Dashed red and solid blue lines represent the spin-up and spin-down channels, respectively. Green and pink circles denote Fe-$d_{x^2-y^2}$ and d_{z^2} orbitals in the spin-down channel. Here, we only focus on analyzing the contribution of d orbitals to the CBM and VBM, and Fig. S7 presents other fatband analysis. Fermi level is set to zero. (c) Calculated spin-polarized charge density of the FeP_4 monolayer, in which blue and yellow represent the different spin states. Diagrammatic sketch of J_1 and J_2 exchange coupling parameters. (d) Variation of the average magnetic moment (M_Z) of the Fe atom (blue) and the specific heat (C_V) (orange) as a function of temperature, derived from Monte Carlo simulations based on the classical Heisenberg model. (e) Angular dependence of the MAE of the FeP_4 monolayer, where the cyan and orange indicate the magnetization in the xy and xz planes, respectively. (f) Orbital-resolved MAE of the Fe atom with respect to the d orbitals.

Table S3. Among them, the FIM ordering has the lowest energy (Table S4). Significantly, the slight lattice deformation leads to the nonequilibrium of the neighboring Fe-Fe distances, namely $d_{Fe1-Fe2} = d_{Fe1-Fe3}$ and $d_{Fe2-Fe4} = d_{Fe3-Fe4}$, driven by the magnetostriction effect, which causes the breaking of rotational symmetry, so that neighboring Fe atoms are no longer equivalent. The spin-unpaired electrons are mainly localized around Fe atoms, indicating that its robust magnetism comes from the partially occupied Fe $3d$ orbital [Fig. 2(c)]. The calculated magnetic moments of the four Fe atoms are Fe1 at $2.23\,\mu_B$, Fe2 at $1.88\,\mu_B$, Fe3 at $1.91\,\mu_B$, and Fe4 at $-2.33\,\mu_B$, which are much lower than the ideal magnetic moment of $4\,\mu_B$ of an isolated Fe atom with the

$3d^6\,4s^2$ electronic configuration, as the strong hybridization between Fe and P reduces the number of unpaired electrons in the Fe $3d$ orbital [Fig. S6(a)].

The calculated spin-polarized band structure and the corresponding spin-resolved projected density of states (PDOS) of FeP_4 clearly shows its half-metallic properties and itinerant magnetism, acting as the messengers to promote the exchange coupling interactions between neighboring local magnetic moments [Figs. 2(a) and 2(b)]. The spin-up bands intersect with the Fermi level and dominate its metallicity, whereas an energy gap of 0.31 eV appears in the spin-down channel, exhibiting a semiconducting character. Therefore, FeP_4 could favor efficient spin-polarized injection and detection spintronics, and benefit promising low-energy spintronic devices, such as magnetoresistive random access memory [79]. The conduction-band minimum (CBM) of the spin-down channel, located at the Γ point, is dominated by the Fe $d^2_{x-y}{}^2$ orbital, and the valence-band maximum (VBM), in the middle of the M–Γ line, presents a contribution of the Fe d^2_z orbital [Fig. 2(a)]. Its magnetism is mainly associated with $d^2_{x-y}{}^2$, d^2_z and double-degenerated d_{xz}/d_{yz} orbitals of Fe atoms [Fig. 2(b)]. On the other hand, as it will be discussed later, the strong hybridization between Fe $3d$ and P $3p$ orbitals [Fig. S6(a)] confirms an indirect magnetic exchange interaction among Fe and P atoms.

The MAE is related to the intrinsic long-range magnetic ordering in 2D materials. Here, in-plane and out-of-plane directions are considered to determine the easy axis. The estimated total energy for the in-plane magnetization is the lowest one. Therefore, the magnetization easy axis of the FeP_4 monolayer lies on the in plane. The angular correlation fit between MAE and the magnetization angle θ/ϕ in the xy/xz plane apparently shows a strong anisotropy [Fig. 2(e)], and the largest MAE reaches 72.55 μeV per Fe atom, which is larger than in bulk Fe (1.4 μeV per atom), Ni (3 μeV per atom) [80], and the VF_4 monolayer (40 μeV per V atom) [81], and comparable to the 2D hematene (87 μeV per Fe atom) and $CoGa_2S_4$ (47 μeV per Co atom) [82,83]. The orbital-resolved MAEs, which account for the relationship between the MAE and d orbitals, are used to explore the origin of the large magnetic anisotropy [Fig. 2(f)], which obviously indicate that the coupling between d_{xz} and d_{yz} orbitals is much stronger than with the other ones. In general, a large MAE plays an important role in keeping the intrinsic long-range magnetic ordering in 2D materials.

The Curie temperature (T_C), which shows the thermal threshold for a transition from a ferromagnetic/ferrimagnetic ordering to a paramagnetic one, was calculated by performing Monte Carlo (MC) simulations based on the classical Heisenberg model. In general, Curie temperatures above room temperature are needed for potential applications. The relative spin Hamiltonian is defined as

$$\hat{H} = -\sum_{ij} J_1 \overrightarrow{S_i}\,\overrightarrow{S_j} - \sum_{ik} J_2 \overrightarrow{S_i}\,\overrightarrow{S_k} - A\left(S_i^z\right)^2,$$

where J_1 and J_2 are defined as the exchange coupling parameters between the neighboring magnetic atoms in Fig. 2(c), representing the nearest-neighbor and next-nearest neighbor magnetic exchange integrals, respectively. Note that the positive and negative J represent the FM and AFM coupling, respectively. $\vec{S}$ represents the spin quantum number of magnetic Fe atoms, while the $(i,\ j)$ and $(i,\ k)$ mean the nearest- and next-nearest Fe sites, respectively. A is the anisotropy energy parameter, and S_i^z is the spin component parallel to the z direction. Details of the mapping of total energies of different spin configurations can be found in the Supplemental Material [61]. The resulting computed parameters of the magnetic exchange couplings are $J_1 = 70.19$ meV and $J_2 = -59.81$ meV, which correspond well to the different spin states between different Fe atoms in the FIM state [Fig. 2(c)]. For magnetic materials the Curie temperature (T_C) is proportional to the magnetic exchange integral. In the other words, the stronger the magnetic exchange is, the greater the parallel orientation capacity of the spins, and the greater the thermal energy required to destroy the regular arrangement in the magnet; that is, the material macroscopically would show a high T_C. Hence, as shown in Fig. 2(d), the estimated T_C by performing MC simulations on a 32×32 2D tetragonal spin supercell of the FeP_4 monolayer is around 460 K, which is considerably higher than room temperature (∼300 K) and T_C s of recently reported 2D FIM materials, such as $Mo_3N_2F_3$ (237 K), organometallic frameworks $K_3M_2[P_CMO_8]$ (M = Mn, Fe, Co) (66∼150 K), and 2D-Cr-DPP (316 K) [24,26,84]. Therefore, the calculated high T_C in the predicted ferrimagnetic FeP_4 monolayer is highly desirable for spintronics.

Subsequently, we try to explore the relationship between ferrimagnetism and the unique P_4 units in FeP_4. First, we tried to break the integrity of the P_4 unit by removing one P atom in a 2×2 supercell [Figs. S8(a) and S8(b)]. The magnetic moment of the Fe atom, closest to the removed P atom, increases to 2.77 μ_B. On the other hand, the next-nearest neighbor coupling, J_1, decreases sharply by 91.7% from 70.19 to 5.82 meV, whereas the next-nearest neighbor coupling, J_2, becomes a positive value. More interestingly, the magnetic ground state changes into a ferromagnetic configuration, and the value of T_C drops to 47 K. Then, we also considered another situation by removing the two P atoms on the diagonal in a P_4 unit [Figs. S8(c) and S8(d)]. In detail, J_1 shows a negative value of −10.96 meV and T_C becomes 83 K. All in all, destroying the integrity of the P_4 unit makes the magnetic exchange interaction weaken significantly, and the magnetic state change accordingly. Due to the strong hybridization of p states between adjacent P atoms in the P_4 unit, which is supported by the strong interaction between p_x, p_y, and p_z orbitals of the two neighboring P atoms (Fig. S9), stabilizing the FIM state and allowing them to act as intermediaries to make it an efficient electron-transferring pathway as will be mentioned below. In other words, the presence of the P_4 unit as an intermediate not only promotes the indirect magnetic exchange interaction in FeP_4, but also remarkably maintains the ferrimagnetic characteristics and the high T_C in the system.

Here, we turn our attention to revealing the microscopic mechanism of the magnetic exchange interaction. For the nearest-neighbor magnetic moments, the longer distance suggests weak direct exchange coupling between neighboring Fe atoms. As mentioned above, the itinerant electrons in the system act as messengers through the medium of the P_4

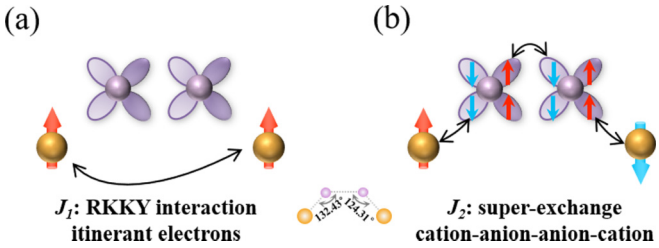

FIG. 3. Possible magnetic exchange types of the (a) nearest-neighbor (J_1) and (b) next-nearest neighbor (J_2) magnetic exchange interactions in the ferrimagnetic FeP_4 monolayer. Golden and pink balls represent Fe and P atoms, respectively. Red, blue, and black arrows represent different spin states and possible pathways for specific electron transferring. Around P atoms are p_x and p_y orbitals with different phase forms.

units, spreading the exchange coupling interactions between two local magnetic moments on Fe ions [Fig. 3(a)], which is known as the Ruderman-Kittel-Kasuya-Yosida (RKKY) interaction. In the RKKY-type interaction, the sign of J oscillates with respect to the distance between the magnetic atoms. Therefore, we have examined the exchange parameter as a function of the Fe-Fe distance by applying biaxial strains from −4 to 6% to change the distance between Fe atoms. As shown in Fig. S10, the calculated magnetic exchange fluctuates between the FIM/FM and AFM coupling with respect to the change in the nearest-neighbor Fe-Fe distance, consistent with the RKKY interaction, which enhances the FM coupling between nearest-neighbor Fe atoms. Unlike the direct electron transferring between the nearest magnetic ions, there is also the possibility of electron transferring due to the superexchange mediated by one or two anions, forming both cation-anion-cation and extended cation-anion-anion-cation interaction channels [85]. It is important to note that the cation-anion-anion-cation exchange interaction depends on both the cation-anion-anion and anion-anion-cation angles. The relevant superexchange electron-transferring pathway for a FeP_4 monolayer is displayed in Fig. 3(b). Based on the Goodenough-Kanamori-Anderson rule [86–88], we can conclude that the superexchange of a bond angle of 90° favors the FM coupling, while those with 180° prefer the AFM coupling. However, numerous reported studies have shown that the AFM order is also preferred when there is a large cation-anion-cation angle (larger than 130°) [89,90]. As shown in Fig. 3(b), the cation-anion-anion and anion-anion-cation bond angles between the next-nearest neighbor Fe ions are much close to 130° and the involved p orbitals of P anions revealed a strong hybridization [see Fig. S6(b)], which presents a strong AFM contribution. As a consequence, the FeP_4 monolayer tends to ferromagnetic ordering in the nearest neighbor while antiferromagnetic ordering between next-nearest neighbor; hence, the ground state shows a ferrimagnetic configuration with the obvious unbalanced spins, which is quite different from the traditional ferrimagnet with unbalanced antiparallel-aligned sublattice moments [9].

On the other hand, strain engineering, which can be achieved by a modulating substrate, has been widely used to improve magnetic and electronic properties of 2D materials in order to improve their spintronic applications [32,33].

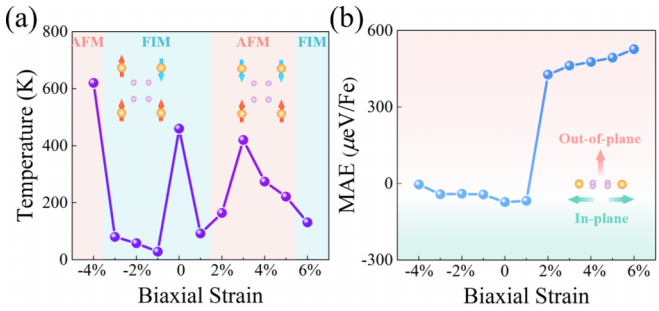

FIG. 4. (a) Magnetic transition temperatures (T_C/T_N) and (b) MAEs of the FeP_4 monolayer under different external biaxial strain.

Therefore, we have applied biaxial strains from −4 to 6% on the FeP_4 monolayer to explore its potential effect on its magnetism, where stretching and compression strains are represented with positive and negative values, respectively. Interestingly, P_4 units can maintain their integrity throughout the whole deformation process. Besides, we find that the magnetism is sensitive to the strains. Specifically, slight tensile strain (∼2%) to the FeP_4 monolayer induces a FIM-AFM phase transition. Then, the magnetic ground state undergoes an AFM to FIM transition under tensile strain of 6%. On the other hand, the FIM coupling configuration of the FeP_4 monolayer is maintained with an increased compressive strain from 0 to −3%, while a magnetic phase transition occurs under a −4% strain, exhibiting an AFM ordering. It is well known that J is determined by the energy difference between FM, FIM, and AFM states. The changing energy difference with strain induces the change of J and magnetic transition temperature [see Fig. 4(a) and Table S5]. Therefore, the strain-induced different magnetic ground states are the origin of the magnetic phase transition, indicating that the magnetism of FeP_4 can be manipulated by adjusting the magnetic coupling interaction strength between the neighboring Fe atoms. With decreasing strain from 6 to −4%, the magnetic moment of the Fe atom first drops monotonically and then increases mildly (Fig. S11), and the enhancement of Fe–Fe bonds and magnetism favors the magnetic exchange interaction of adjacent Fe atoms (Table S5). Here, most of magnetic transition temperatures (T_C/T_N) can be maintained at high temperatures, especially when compressed by −4%, the T_N is as high as 620 K [Figs. 4(a) and S12]. Meanwhile, upon stretching, the FeP_4 monolayer prefers the out-of-plane alignment of spins under the external strain from 2 to 6% with a high perpendicular MAE reaching 526 μeV/Fe at 6% tensile strain. In addition, the in-plane easy axis remains at the compressive strains from 1 to −4% [see Fig. 4(b)].

IV. CONCLUSIONS

In summary, we apply first-principles structural search calculations to predict a FIM FeP_4 monolayer with intrinsic half metallicity and high dynamical, thermal, and mechanical stabilities, associated with its unique atomic configurations. The FeP_4 monolayer is a robust ferrimagnet with a high T_C of 460 K, large in-plane MAE, and full spin polarization, where the magnetism is mainly derived from the unfilled Fe-d orbital. Besides, P_4 units promote the superexchange interaction

while itinerant electrons support the RKKY interaction, responsible for its robust ferrimagnetism. Under external biaxial strain, there is a transition from ferrimagnetism to antiferromagnetism and, upon stretching, the magnetic easy axis changes to out-of-plane. These excellent properties make the FeP_4 monolayer have great potential for applications in high-performance spintronics nanodevices.

ACKNOWLEDGMENTS

The authors acknowledge the funding support from the Natural Science Foundation of China under Grants No. 21873017 and No. 21573037, the Postdoctoral Science Foundation of China under Grant No. 2013M541283, the Natural Science Foundation of Jilin Province (Grant No. 20190201231JC), and the Natural Science Foundation of Hebei Province (Grant No. B2021203030), the Science and Technology Project of Hebei Education Department (Grant No. JZX2023020). The work was carried out at National Supercomputer Center in Tianjin, and the calculations were performed on TianHe-1 (A). A.B. acknowledges financial support from the Spanish Ministry of Science and Innovation (Grant No. PID2019-105488GB-I00) and the Department of Education, Universities and Research of the Basque Government and the University of the Basque Country (Grant No. IT1707-22).

The authors declare no competing financial interest.

[1] S. Bhatti, R. Sbiaa, A. Hirohata, H. Ohno, S. Fukami, and S. N. Piramanayagam, Spintronics based random access memory: A review, Mater. Today **20**, 530 (2017).

[2] I. Žutić, J. Fabian, and S. Das Sarma, Spintronics: Fundamentals and applications, Rev. Mod. Phys. **76**, 323 (2004).

[3] X. Li and J. Yang, First-principles design of spintronics materials, Natl. Sci. Rev. **3**, 365 (2016).

[4] A. Fert, The present and the future of spintronics, Thin Solid Films **517**, 2 (2008).

[5] T. Jungwirth, X. Marti, P. Wadley, and J. Wunderlich, Antiferromagnetic spintronics, Nat. Nanotechnol. **11**, 231 (2016).

[6] V. Baltz, A. Manchon, M. Tsoi, T. Moriyama, T. Ono, and Y. Tserkovnyak, Antiferromagnetic spintronics, Rev. Mod. Phys. **90**, 015005 (2018).

[7] T. Jungwirth, J. Sinova, A. Manchon, X. Marti, J. Wunderlich, and C. Felser, The multiple directions of antiferromagnetic spintronics, Nat. Phys. **14**, 200 (2018).

[8] C. Chappert, A. Fert, and F. N. Van Dau, The emergence of spin electronics in data storage, Nat. Mater. **6**, 813 (2007).

[9] S. K. Kim, G. S. D. Beach, K.-J. Lee, T. Ono, T. Rasing, and H. Yang, Ferrimagnetic spintronics, Nat. Mater. **21**, 24 (2022).

[10] A. A. Serga, A. V Chumak, and B. Hillebrands, YIG magnonics, J. Phys. D: Appl. Phys. **43**, 264002 (2010).

[11] R. Sharma, P. Thakur, P. Sharma, and V. Sharma, Ferrimagnetic Ni^{2+} doped Mg-Zn spinel ferrite nanoparticles for high density information storage, J. Alloys Compd. **704**, 7 (2017).

[12] I. Galanakis, K. Özdoğan, E. Şaşıoğlu, and B. Aktaş, *Ab initio* design of half-metallic fully compensated ferrimagnets: The case of Cr_2MnZ (Z = P, As, Sb, and Bi), Phys. Rev. B **75**, 172405 (2007).

[13] B. Huang, G. Clark, E. Navarro-Moratalla, D. R. Klein, R. Cheng, K. L. Seyler, D. Zhong, E. Schmidgall, M. A. McGuire, D. H. Cobden, W. Yao, D. Xiao, P. Jarillo-Herrero, and X. Xu, Layer-dependent ferromagnetism in a van der Waals crystal down to the monolayer limit, Nature (London) **546**, 270 (2017).

[14] C. Gong, L. Li, Z. Li, H. Ji, A. Stern, Y. Xia, T. Cao, W. Bao, C. Wang, Y. Wang, Z. Q. Qiu, R. J. Cava, S. G. Louie, J. Xia, and X. Zhang, Discovery of intrinsic ferromagnetism in two-dimensional van der Waals crystals, Nature (London) **546**, 265 (2017).

[15] Z. Zhang, J. Shang, C. Jiang, A. Rasmita, W. Gao, and T. Yu, Direct photoluminescence probing of ferromagnetism in monolayer two-dimensional $CrBr_3$, Nano Lett. **19**, 3138 (2019).

[16] M. Nakano, Y. Wang, S. Yoshida, H. Matsuoka, Y. Majima, K. Ikeda, Y. Hirata, Y. Takeda, H. Wadati, Y. Kohama, Y. Ohigashi, M. Sakano, K. Ishizaka, and Y. Iwasa, Intrinsic 2D ferromagnetism in V_5Se_8 epitaxial thin films, Nano Lett. **19**, 8806 (2019).

[17] K. Kim, S. Y. Lim, J. Kim, J.-U. Lee, S. Lee, P. Kim, K. Park, S. Son, C.-H. Park, J.-G. Park, and H. Cheong, Antiferromagnetic ordering in van der Waals 2D magnetic material $MnPS_3$ probed by Raman spectroscopy, 2D Mater. **6**, 41001 (2019).

[18] S. Tian, J.-F. Zhang, C. Li, T. Ying, S. Li, X. Zhang, K. Liu, and H. Lei, Ferromagnetic van der Waals crystal VI_3, J. Am. Chem. Soc. **141**, 5326 (2019).

[19] D. Yujun, Y. Yijun, S. M. Zhu, G. Zhongxun, X. Zihan, W. Jing, C. X. Hui, and Z. Yuanbo, Quantum anomalous Hall effect in intrinsic magnetic topological insulator $MnBi_2Te_4$, Science **367**, 895 (2020).

[20] M. Bonilla, S. Kolekar, Y. Ma, H. C. Diaz, V. Kalappattil, R. Das, T. Eggers, H. R. Gutierrez, M.-H. Phan, and M. Batzill, Strong room-temperature ferromagnetism in VSe_2 monolayers on van der Waals substrates, Nat. Nanotechnol. **13**, 289 (2018).

[21] X. Sun, W. Li, X. Wang, Q. Sui, T. Zhang, Z. Wang, L. Liu, D. Li, S. Feng, S. Zhong, H. Wang, V. Bouchiat, M. Nunez Regueiro, N. Rougemaille, J. Coraux, A. Purbawati, A. Hadj-Azzem, Z. Wang, B. Dong, X. Wu, T. Yang, G. Yu, B. Wang, Z. Han, X. Han, and Z. Zhang, Room temperature ferromagnetism in ultra-thin van der Waals crystals of 1T-$CrTe_2$, Nano Res. **13**, 3358 (2020).

[22] Y. Wen, Z. Liu, Y. Zhang, C. Xia, B. Zhai, X. Zhang, G. Zhai, C. Shen, P. He, R. Cheng, L. Yin, Y. Yao, M. Getaye Sendeku, Z. Wang, X. Ye, C. Liu, C. Jiang, C. Shan, Y. Long, and J. He, Tunable room-temperature ferromagnetism in two-dimensional Cr_2Te_3, Nano Lett. **20**, 3130 (2020).

[23] F. Cui, X. Zhao, J. Xu, B. Tang, Q. Shang, J. Shi, Y. Huan, J. Liao, Q. Chen, Y. Hou, Q. Zhang, S. J. Pennycook, and Y. Zhang, Controlled growth and thickness-dependent conduction-type transition of 2D ferrimagnetic Cr_2S_3 semiconductors, Adv. Mater. **32**, 1905896 (2020).

[24] X. Li, X. Li, and J. Yang, Two-dimensional multifunctional metal–organic frameworks with simultaneous ferro-/ferrimagnetism and vertical ferroelectricity, J. Phys. Chem. Lett. **11**, 4193 (2020).

[25] X. Li and J. Yang, Realizing two-dimensional magnetic semiconductors with enhanced Curie temperature by antiaromatic

ring based organometallic frameworks, J. Am. Chem. Soc. **141**, 109 (2019).

[26] S. Li, S. Hu, W. Ji, P. Li, K. Zhang, C. Zhang, and S. Yan, Emergence of ferrimagnetic half-metallicity in two-dimensional MXene $Mo_3N_2F_2$, Appl. Phys. Lett. **111**, 202405 (2017).

[27] D. Wu, Z. Zhuo, H. Lv, and X. Wu, Two-dimensional $Cr_2X_3S_3$(X = Br, I) Janus semiconductor with intrinsic room-temperature magnetism, J. Phys. Chem. Lett. **12**, 2905 (2021).

[28] Y. Ren, L. Hu, Y. Shao, Y. Hu, L. Huang, and X. Shi, Magnetism of elemental two-dimensional metals, J. Mater. Chem. C **9**, 4554 (2021).

[29] A. M. Turner, A. W. Donoho, and J. L. Erskine, Experimental bulk electronic properties of ferromagnetic iron, Phys. Rev. B **29**, 2986 (1984).

[30] Y. Deng, Y. Yu, Y. Song, J. Zhang, N. Z. Wang, Z. Sun, Y. Yi, Y. Z. Wu, S. Wu, J. Zhu, J. Wang, X. H. Chen, and Y. Zhang, Gate-tunable room-temperature ferromagnetism in two-dimensional Fe_3GeTe_2, Nature (London) **563**, 94 (2018).

[31] P. A. Joy and S. Vasudevan, Magnetism in the layered transition-metal thiophosphates MPS_3 (M = Mn, Fe, and Ni), Phys. Rev. B **46**, 5425 (1992).

[32] Y. Sun, Z. Zhuo, X. Wu, and J. Yang, Room-temperature ferromagnetism in two-dimensional Fe_2Si nanosheet with enhanced spin-polarization ratio, Nano Lett. **17**, 2771 (2017).

[33] S. Zheng, C. Huang, T. Yu, M. Xu, S. Zhang, H. Xu, Y. Liu, E. Kan, Y. Wang, and G. Yang, High-temperature ferromagnetism in Fe_3P monolayer with large magnetic anisotropy, J. Phys. Chem. Lett. **10**, 2733 (2019).

[34] C. Tang, K. (Ken) Ostrikov, S. Sanvito, and A. Du, Prediction of room-temperature ferromagnetism and large perpendicular magnetic anisotropy in a planar hypercoordinate FeB_3 monolayer, Nanoscale Horizons **6**, 43 (2021).

[35] H.-Y. Cao, S. Chen, H. Xiang, and X.-G. Gong, Antiferromagnetic ground state with pair-checkerboard order in FeSe, Phys. Rev. B **91**, 020504(R) (2015).

[36] K. Zhang, M. Chen, D. Wang, H. Lv, X. Wu, and J. Yang, Nodal-loop half metallicity in a two-dimensional Fe_4N_2 pentagon crystal with room-temperature ferromagnetism, Nanoscale **13**, 19493 (2021).

[37] C. Huang, Y. Du, H. Wu, H. Xiang, K. Deng, and E. Kan, Prediction of Intrinsic Ferromagnetic Ferroelectricity in a Transition-Metal Halide Monolayer, Phys. Rev. Lett. **120**, 147601 (2018).

[38] C. Huang, J. Feng, F. Wu, D. Ahmed, B. Huang, H. Xiang, K. Deng, and E. Kan, Toward intrinsic room-temperature ferromagnetism in two-dimensional semiconductors, J. Am. Chem. Soc. **140**, 11519 (2018).

[39] C. Huang, J. Feng, J. Zhou, H. Xiang, K. Deng, and E. Kan, Ultra-high-temperature ferromagnetism in intrinsic tetrahedral semiconductors, J. Am. Chem. Soc. **141**, 12413 (2019).

[40] M. Batmunkh, M. Bat-Erdene, and J. G. Shapter, Phosphorene and phosphorene-based materials–prospects for future applications, Adv. Mater. **28**, 8586 (2016).

[41] H. Liu, A. T. Neal, Z. Zhu, Z. Luo, X. Xu, D. Tománek, and P. D. Ye, Phosphorene: An unexplored 2D semiconductor with a high hole mobility, ACS Nano **8**, 4033 (2014).

[42] B. Liu, M. Köpf, A. N. Abbas, X. Wang, Q. Guo, Y. Jia, F. Xia, R. Weihrich, F. Bachhuber, F. Pielnhofer, H. Wang, R. Dhall, S. B. Cronin, M. Ge, X. Fang, T. Nilges, and C. Zhou, Black arsenic–phosphorus: Layered anisotropic infrared semiconductors with highly tunable compositions and properties, Adv. Mater. **27**, 4423 (2015).

[43] Z. Wang, P. Luo, B. Han, X. Zhang, S. Zhao, S. Wang, X. Chen, L. Wei, S. Yang, X. Zhou, S. Wang, X. Tao, and T. Zhai, Strong in-plane anisotropic SiP_2 as a IV–V 2D semiconductor for polarized photodetection, ACS Nano **15**, 20442 (2021).

[44] Y. Liu, R. Wang, Z. Wang, D. Li, and T. Cui, Formation of twelve-fold iodine coordination at high pressure, Nat. Commun. **13**, 412 (2022).

[45] W. Lu, S. Liu, G. Liu, K. Hao, M. Zhou, P. Gao, H. Wang, J. Lv, H. Gou, G. Yang, Y. Wang, and Y. Ma, Disproportionation of SO_2 at High Pressure and Temperature, Phys. Rev. Lett. **128**, 106001 (2022).

[46] Y. Wang, J. Lv, L. Zhu, and Y. Ma, CALYPSO: A method for crystal structure prediction, Comput. Phys. Commun. **183**, 2063 (2012).

[47] Y. Wang, J. Lv, L. Zhu, and Y. Ma, Crystal structure prediction via particle-swarm optimization, Phys. Rev. B **82**, 094116 (2010).

[48] Y. Wang, M. Xu, L. Yang, B. Yan, Q. Qin, X. Shao, Y. Zhang, D. Huang, X. Lin, J. Lv, D. Zhang, H. Gou, H. Mao, C. Chen, and Y. Ma, Pressure-stabilized divalent ozonide CaO_3 and its impact on earth's oxygen cycles, Nat. Commun. **11**, 4702 (2020).

[49] M. Miao, Y. Sun, E. Zurek, and H. Lin, Chemistry under high pressure, Nat. Rev. Chem. **4**, 508 (2020).

[50] J. Jang, G. H. Gu, J. Noh, J. Kim, and Y. Jung, Structure-based synthesizability prediction of crystals using partially supervised learning, J. Am. Chem. Soc. **142**, 18836 (2020).

[51] Y. Yu, J. Zhou, and Z. Sun, Novel 2D transition-metal carbides: Ultrahigh performance electrocatalysts for overall water splitting and oxygen reduction, Adv. Funct. Mater. **30**, 2000570 (2020).

[52] M. Xu, C. Huang, Y. Li, S. Liu, X. Zhong, P. Jena, E. Kan, and Y. Wang, Electrical Control of Magnetic Phase Transition in a Type-I Multiferroic Double-Metal Trihalide Monolayer, Phys. Rev. Lett. **124**, 067602 (2020).

[53] S. M. Woodley and R. Catlow, Crystal structure prediction from first principles, Nat. Mater. **7**, 937 (2008).

[54] N. A. W. Holzwarth, A. R. Tackett, and G. E. Matthews, A Projector Augmented Wave (PAW) code for electronic structure calculations, Part I: Atompaw for generating atom-centered functions, Comput. Phys. Commun. **135**, 329 (2001).

[55] A. E. Mattsson, R. Armiento, P. A. Schultz, and T. R. Mattsson, Nonequivalence of the generalized gradient approximations PBE and PW91, Phys. Rev. B **73**, 195123 (2006).

[56] X. Wu and S. Qin, First-principles calculations of the structural stability of Fe_2P, J. Phys. Conf. Ser. **215**, 12110 (2010).

[57] A. Togo, F. Oba, and I. Tanaka, First-principles calculations of the ferroelastic transition between rutile-type and $CaCl_2$−Type SiO_2 at high pressures, Phys. Rev. B **78**, 134106 (2008).

[58] Y. Zhang and E. J. Maginn, A simple AIMD approach to derive atomic charges for condensed phase simulation of ionic liquids, J. Phys. Chem. B **116**, 10036 (2012).

[59] V. Wang, N. Xu, J.-C. Liu, G. Tang, and W.-T. Geng, VASPKIT: A user-friendly interface facilitating high-throughput computing and analysis using VASP code, Comput. Phys. Commun. **267**, 108033 (2021).

[60] L. Liu, X. Ren, J. Xie, B. Cheng, W. Liu, T. An, H. Qin, and J. Hu, Magnetic switches via electric field in BN nanoribbons, Appl. Surf. Sci. **480**, 300 (2019).

[61] See Supplemental Material at http://link.aps.org/supplemental/10.1103/PhysRevB.107.024414 for the theoretical methods, structural stabilities, geometric, electronic, and magnetic details, different magnetic configurations with corresponding energies, calculations of magnetic behavior of the FeP_4 monolayer with incomplete P_4 unit, magnetic exchange parameters (J_1) and magnetic transition temperatures of FeP_4 monolayer under biaxial strains, the integrated COHP (ICOHP), and structural information, which includes Refs. [62–71].

[62] G. Kresse and J. Furthmüller, Efficient iterative schemes for ab initio total-energy calculations using a plane-wave basis set, Phys. Rev. B **54**, 11169 (1996).

[63] W. Kohn and L. J. Sham, Self-consistent equations including exchange and correlation effects, Phys. Rev. **140**, A1133 (1965).

[64] J. P. Perdew, K. Burke, and M. Ernzerhof, Generalized Gradient Approximation Made Simple, Phys. Rev. Lett. **77**, 3865 (1996).

[65] H. J. Monkhorst and J. D. Pack, Special points for Brillouin-zone integrations, Phys. Rev. B. **13**, 5188 (1976).

[66] C. Yan, J. Yi, D. Li, C. Xu, and L. Cheng, FeP_2 monolayer: Isoelectronic analogue of MoS_2 with excellent electronic and optical properties, Phys. Chem. Chem. Phys. **24**, 13376 (2022).

[67] N. Lu, Z. Zhuo, H. Guo, P. Wu, W. Fa, X. Wu, and X. C. Zeng, CaP_3: A new two-dimensional functional material with desirable band gap and ultrahigh carrier mobility, J. Phys. Chem. Lett. **9**, 1728 (2018).

[68] A. Simon, H. Borrmann, and H. Craubner, Crystal structure of ordered white phosphorus(β-P), Phosphorus Sulfur Relat. Elem. **30**, 507 (1987).

[69] X.-B. Li, P. Guo, T.-F. Cao, H. Liu, W.-M. Lau, and L.-M. Liu, Structures, stabilities and electronic properties of defects in monolayer black phosphorus, Sci. Rep. **5**, 10848 (2015).

[70] Z. Zhu and D. Tománek, Semiconducting Layered Blue Phosphorus: A Computational Study, Phys. Rev. Lett. **112**, 176802 (2014).

[71] J. Guan, Z. Zhu, and D. Tománek, Phase Coexistence and Metal-Insulator Transition in Few-Layer Phosphorene: A Computational Study, Phys. Rev. Lett. **113**, 046804 (2014).

[72] S. Zheng, T. Yu, J. Lin, H. Lou, H. Xu, and G. Yang, FeP_3 Monolayer as a high-efficiency catalyst for hydrogen evolution reaction, J. Mater. Chem. A **7**, 25665 (2019).

[73] S. Zhao, Z. Li, and J. Yang, Obtaining two-dimensional electron gas in free space without resorting to electron doping: An electride based design, J. Am. Chem. Soc. **136**, 13313 (2014).

[74] Y. Jing, Y. Ma, Y. Li, and T. Heine, GeP_3: A small indirect band gap 2D crystal with high carrier mobility and strong interlayer quantum confinement, Nano Lett. **17**, 1833 (2017).

[75] Y. Cai, Q. Ke, G. Zhang, Y. P. Feng, V. B. Shenoy, and Y. W. Zhang, Giant phononic anisotropy and unusual anharmonicity of phosphorene: Interlayer coupling and strain engineering, Adv. Funct. Mater. **25**, 2230 (2015).

[76] M. Born and K. Huang, Dynamical theory of crystal lattices, Am. J. Phys. **23**, 474 (1955).

[77] Z. Shunhong, Z. Jian, W. Qian, C. Xiaoshuang, K. Yoshiyuki, and J. Puru, Penta-graphene: A new carbon allotrope, Proc. Natl. Acad. Sci. USA **112**, 2372 (2015).

[78] X. Xu, Y. Ma, T. Zhang, C. Lei, B. Huang, and Y. Dai, Prediction of two-dimensional antiferromagnetic ferroelasticity in an AgF_2 monolayer, Nanoscale Horizons **5**, 1386 (2020).

[79] W. Kim, K. Kawaguchi, N. Koshizaki, M. Sohma, and T. Matsumoto, Fabrication and magnetoresistance of tunnel junctions using half-metallic Fe_3O_4, J. Appl. Phys. **93**, 8032 (2003).

[80] G. H. O. Daalderop, P. J. Kelly, and M. F. H. Schuurmans, First-principles calculation of the magnetocrystalline anisotropy energy of iron, cobalt, and nickel, Phys. Rev. B **41**, 11919 (1990).

[81] L. Zhang, C. Tang, and A. Du, Two-dimensional vanadium tetrafluoride with antiferromagnetic ferroelasticity and bidirectional negative Poisson's ratio, J. Mater. Chem. C **9**, 95 (2021).

[82] R. Singla, T. A. Hackett, S. Kumar, J. Sharma, and M. K. Kashyap, Curie temperature engineering in a novel 2D analog of iron ore (hematene) via strain, Nanoscale Adv. **2**, 5890 (2020).

[83] S. Zhang, R. Xu, W. Duan, and X. Zou, Intrinsic half-metallicity in 2D ternary chalcogenides with high critical temperature and controllable magnetization direction, Adv. Funct. Mater. **29**, 1808380 (2019).

[84] X. Li and J. Yang, Toward room-temperature magnetic semiconductors in two-dimensional ferrimagnetic organometallic lattices, J. Phys. Chem. Lett. **10**, 2439 (2019).

[85] W.-B. Zhang, Q. Qu, P. Zhu, and C.-H. Lam, Robust intrinsic ferromagnetism and half semiconductivity in stable two-dimensional single-layer chromium trihalides, J. Mater. Chem. C **3**, 12457 (2015).

[86] J. B. Goodenough, Theory of the role of covalence in the perovskite-type manganites La, M(II)MnO_3, Phys. Rev. **100**, 564 (1955).

[87] J. Kanamori, Crystal distortion in magnetic compounds, J. Appl. Phys. **31**, S14 (1960).

[88] P. W. Anderson, New approach to the theory of superexchange interactions, Phys. Rev. **115**, 2 (1959).

[89] M. A. Subramanian, A. P. Ramirez, and W. J. Marshall, Structural Tuning of Ferromagnetism in a 3D Cuprate Perovskite, Phys. Rev. Lett. **82**, 1558 (1999).

[90] D. Zhang, A. Rahman, W. Qin, X. Li, P. Cui, Z. Zhang, and Z. Zhang, Prediction of $MnSiTe_3$ as an intrinsic layered half-metal, Phys. Rev. B **101**, 205119 (2020).